

On Calibration and Validation of Eigendefor- mation-Based Multiscale Models for Failure Analysis of Heterogeneous Systems

Caglar Oskay

Civil and Environmental Engineering Department
Vanderbilt University
Nashville, TN, 37235

Jacob Fish

Mechanical, Aerospace and Nuclear Engineering Department
Rensselaer Polytechnic Institute
Troy, NY, 12180

Abstract

We present a new strategy for calibration and validation of hierarchical multiscale models based on computational homogenization. The proposed strategy hinges on the concept of the experimental simulator repository (SIMEX) which provides the basis for a generic algorithmic framework in calibration and validation of multiscale models. Gradient-based and genetic algorithms are incorporated into SIMEX framework to investigate the validity of these algorithms in multiscale model calibration. The strategy is implemented using the eigendefor- mation-based reduced order homogenization (EHM) model and integrated into a commercial finite element package (Abaqus). Ceramic- and polymer- matrix composite problems are analyzed to study the capabilities of the proposed calibration and validation framework.

1 Introduction

This paper is concerned with the development of calibration and validation procedures for hierarchical multiscale models. We particularly concentrate on validation of eigendefor- mation-based reduced order computational homogenization method (EHM) developed by the authors in [1]. EHM has its roots in mathematical homogenization theory with eigenstrains [2, 3, 4] and transformation field analysis [5, 6, 7], but extends these methods to incorporate interface failure and model adaptivity.

We adopt the definition of *validation* introduced by Babuska and Oden [8] as “the process of determination whether a mathematical model of a physical event represent physical events with sufficient accuracy”. Hierarchical multiscale models based on mathematical homogeniza- tion are the mathematical model space of interest, and the physical event is defined as the

failure of heterogeneous systems subjected to mechanical or thermal loads. The relative accuracy is considered to be the discrepancy between the experimental observations of a certain quantity of interest (such as the uniaxial stress-strain response in case of a uniaxial tension test) and the predictions of a *calibrated* multiscale model. Calibration process is defined as the estimation of material parameters by minimizing the discrepancy between numerical simulations and calibration experiments which are separate and independent of the experiments used for validation purposes. One primary objective of this manuscript is to formulate a strategy for calibration of hierarchical multiscale models with particular emphasis on the EHM model. Multiscale model calibration present distinct challenges compared to that of *phenomenological* models. Calibration of phenomenological models is a relatively straightforward task: typically, experimental techniques are tailored to estimate a single (or a small set of) phenomenological parameter defined at the macroscopic scale. In contrast, material parameters associated with multiscale models are defined at fine scales, often orders of magnitude smaller than the scale at which experiments are conducted. For some heterogeneous systems, calibration based on virgin properties of microconstituents were shown to be satisfactory [9]. On many others, virgin properties may differ significantly from in-situ properties [10]. When virgin and in-situ properties markedly differ from each other, calibrations must be conducted simultaneously for all (or large sets of) microconstituent material parameters that affect predictions at the coarse scale.

The traditional paradigm for evaluation of best material parameter set is gradient-based optimization. This approach typically converges quadratically when the following criteria is satisfied: (a) close proximity of the initial guess to the global minimum; (b) smoothness of the objective function for computability; and (c) convexity. While criteria (b) and (c) are typically satisfied for PDE-based optimization problems to satisfy existence and uniqueness properties of the forward problem, the failure of criterion (a) generally leads to premature convergence to local minima. This problem is alleviated by invoking the gradient-based algorithms from multiple randomly chosen initial guesses and selecting the smallest of the computed optimal minima. Genetic type evolutionary algorithms present an alternative paradigm for the evaluation of globally optimal material parameter set. While the fundamental ideas are based on evolutionary biology, such algorithms were shown to be effective in evaluating various optimization problems in science, engineering and information technology [11, 12].

In this manuscript, we present a new strategy for calibration of hierarchical multiscale models. In the proposed approach, the concept of an experiment simulator (SIMEX) repository is devised, which is a collection of program modules tasked to simulate a particular experimental setup. SIMEX based validation strategy proposed here has the following characteristics:

1. The experiment simulator repository is fully extensible: incorporation of additional experimental setups is trivial;
2. The algorithm is implemented around a commercial finite element software; and,
3. It allows for calibration of an arbitrary subset of the material parameters pertinent to the model based on an arbitrary subset of the available experimental results.

The calibration of the multiscale models were conducted using gradient-based and evolutionary (i.e., genetic) optimization algorithms with the objectives of improving the reliability of the calibrated material parameters, and assessing the validity of these algorithms in evaluating the optimal set of material parameters. The optimizations are focused on exploring the parameter space associated with the microstructural constituents of heterogeneous materials. The proposed calibration and validation strategy is implemented for the EHM method. The

capabilities of the strategy are demonstrated by the analysis of ceramic- and polymer-matrix composite systems.

This manuscript is organized as follows: In Section 2, we review the governing equations for the eigendeformation-based reduced order homogenization method in the context of rate-independent and rate-dependent damage mechanics, and discuss the model reduction methodology. In Section 3, the calibration strategy for the reduced order models is proposed. The implementation of the proposed calibration and validation strategies are discussed in detail and a general computer code structure for calibration and validation of multiscale models are described. Chapter 4 presents calibration and validation examples on ceramic and polymer matrix composites. We conclude with a summary and discussion of the future work.

2 Eigendeformation-Based Homogenization

Consider a macroscopic domain, Ω , with a locally periodic heterogeneous microstructure of arbitrary complexity. Domain of the microstructure, Θ , is composed of one (or more) reinforcing inclusion phase in addition to the surrounding matrix (Fig. 1). The interfaces between the microstructural phases are denoted by S . The ratio between the characteristic lengths of the microstructure and macrostructure is assumed to be small.

When subjected to mechanical loads, the heterogeneous body undergoes inelastic deformations and damage in the form of microcrack formation, growth and coalescence in addition to debonding along the interfaces. In this manuscript this problem is evaluated by employing the eigendeformation based reduced order homogenization method. The failure of the heterogeneous body is modeled by considering damage within the microconstituents and along the interfaces. Continuous damage mechanics models are employed to represent the state of damage at each phase in addition to the interfaces. The governing equations of the macroscopic boundary value problem associated with the heterogeneous domain are obtained using the eigendeformation-based reduced order homogenization methodology [1]. The momentum balance equation is given by

$$\nabla \cdot \bar{\boldsymbol{\sigma}} + \bar{\mathbf{b}} = \bar{\rho} \ddot{\mathbf{u}} \quad (1)$$

in which, $\bar{\boldsymbol{\sigma}}(\mathbf{x}, t)$ is the macroscopic stress tensor; $\mathbf{u}(\mathbf{x}, t)$ the macroscopic displacement field; $\bar{\mathbf{b}}(\mathbf{x}, t)$ the body force; and, $\bar{\rho}(\mathbf{x}, t)$ the macroscopic density. Superposed single and double dot correspond to first and second order material time derivatives, respectively; overbar denotes average over the microstructural domain, Θ ; $\mathbf{x} \in \Omega$ the position vector in the macroscopic domain; and, $t \in [0, t_0]$ the time coordinate. Macroscopic strain tensor, $\bar{\boldsymbol{\epsilon}}(\mathbf{x}, t)$, is expressed in terms of macroscopic displacement field based on the assumption of small deformations (for extension to large deformation we refer to [1])

$$\bar{\boldsymbol{\epsilon}} = \nabla^s \mathbf{u} \quad (2)$$

where ∇^s is the symmetric gradient operator. Initial and boundary conditions are

$$\mathbf{u} = \hat{\mathbf{u}}; \quad t = 0 \quad (3)$$

$$\dot{\mathbf{u}} = \hat{\mathbf{v}}; \quad t = 0 \quad (4)$$

$$\mathbf{u} = \bar{\mathbf{u}}; \quad \mathbf{x} \in \Gamma_u \quad (5)$$

$$\mathbf{n} \cdot \bar{\boldsymbol{\sigma}} = \bar{\mathbf{t}}; \quad \mathbf{x} \in \Gamma_t \quad (6)$$

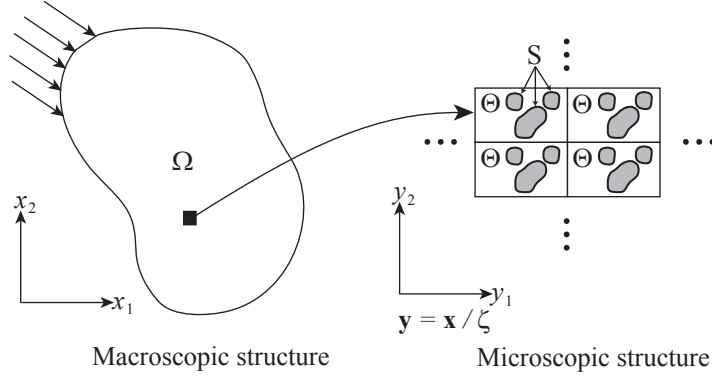


Figure 1: Macroscopic problem domain and microstructure.

in which, $\hat{\mathbf{u}}(\mathbf{x})$ and $\hat{\mathbf{v}}(\mathbf{x})$ are the initial displacement and velocity fields, respectively; $\bar{\mathbf{u}}(\mathbf{x}, t)$ and $\bar{\mathbf{t}}(\mathbf{x}, t)$ are the prescribed displacements and tractions on the boundaries Γ_u and Γ_t , respectively, where $\Gamma = \Gamma_u \cup \Gamma_t$ and $\Gamma_u \cap \Gamma_t = \emptyset$, and; \mathbf{n} is the unit normal to Γ_t .

The constitutive relation for the macroscopic problem is

$$\bar{\boldsymbol{\sigma}} = \bar{\mathbf{L}} : \bar{\boldsymbol{\epsilon}} + \sum_{\beta=1}^m \bar{\mathbf{R}}^{(\beta)} \cdot \hat{\boldsymbol{\delta}}^{(\beta)} + \sum_{\gamma=1}^n \bar{\mathbf{M}}^{(\gamma)} : \boldsymbol{\mu}^{(\gamma)} \quad (7)$$

in which $\hat{\boldsymbol{\delta}}^{(\beta)}(\mathbf{x}, t)$ is the microscopically nonlocal displacement jump vector; and, $\boldsymbol{\mu}^{(\gamma)}(\mathbf{x}, t)$ the microscopically nonlocal inelastic deformation tensor. $\hat{\boldsymbol{\delta}}^{(\beta)}(\mathbf{x}, t)$ and $\boldsymbol{\mu}^{(\gamma)}(\mathbf{x}, t)$ are collectively called eigendeformation, which characterize the effects of the presence of inelastic processes due to accumulation of phase and interface damage; $\bar{\mathbf{R}}^{(\beta)}$, $\bar{\mathbf{L}}$, and $\bar{\mathbf{M}}^{(\gamma)}$ are coefficient tensors which reflect the geometrical effects in the microstructure in addition to the mechanical properties of the associated phases and interfaces. The expressions for $\bar{\mathbf{R}}^{(\beta)}$, $\bar{\mathbf{L}}$, and $\bar{\mathbf{M}}^{(\gamma)}$ are presented in the Appendix. m and n are the number of microscopic phase and interface partitions, respectively. The size and number of phase and interface partitions are evaluated based on the characteristic size within the microstructure and level of model accuracy as further discussed below and in Ref. [1]. The eigendeformation fields are evaluated by solving a system of algebraic equations which are derived from the microscopic boundary value problem of the direct nonlinear homogenization theory (see, for instance, [13, 14, 15]). The algebraic system consists of kinetic and kinematic equations, contact conditions and evolution equations for phase and interface damage variables. Kinetic equation reads

$$\hat{\mathbf{t}}^{(\alpha)} + \sum_{\beta=1}^m \hat{\mathbf{D}}^{(\alpha\beta)} \cdot \hat{\boldsymbol{\delta}}^{(\beta)} + \sum_{\gamma=1}^n \hat{\mathbf{F}}^{(\alpha\gamma)} : \boldsymbol{\mu}^{(\gamma)} = -\hat{\mathbf{C}}^{(\alpha)} : \bar{\boldsymbol{\epsilon}}, \quad \alpha = 1, 2, \dots, m \quad (8)$$

where $\hat{\mathbf{t}}^{(\alpha)}(\mathbf{x}, t)$ is a microscopically nonlocal traction vector; $\hat{\mathbf{D}}^{(\alpha\beta)}$, $\hat{\mathbf{F}}^{(\alpha\gamma)}$ and $\hat{\mathbf{C}}^{(\alpha)}$ are coefficient tensors reflecting the microstructural effects. The expressions for the coefficient tensors are listed in the Appendix. The kinematic equation is given by

$$\sum_{\gamma=1}^n \left[\delta_{\eta\gamma}^{\mathbf{K}} \mathbf{I} - \mathbf{P}(\eta\gamma) \omega_{\text{ph}}^{(\eta)} \right] : \boldsymbol{\mu}^{(\gamma)} - \omega_{\text{ph}}^{(\eta)} \sum_{\beta=1}^m \left[\hat{\mathbf{R}}^{(\eta\beta)} \cdot \hat{\boldsymbol{\delta}}^{(\beta)} \right] = \omega_{\text{ph}}^{(\eta)} \mathbf{A}^{(\eta)} : \bar{\boldsymbol{\epsilon}}, \quad \eta = 1, 2, \dots, n \quad (9)$$

in which, $\omega_{\text{ph}}^{(\eta)}(\mathbf{x}, t)$ is the isotropic, scalar phase damage variable; $\delta_{\eta\gamma}^{\text{K}}$ the Kronecker Delta function; \mathbf{I} the fourth order identity tensor; $\mathbf{P}^{(\eta\gamma)}$, $\hat{\mathbf{R}}^{(\eta\beta)}$ and $\mathbf{A}^{(\eta)}$ are coefficient tensors listed in the Appendix.

Progressive debonding along the microconstituent interfaces is modeled using Continuous Damage Mechanics (CDM). The state of adhesion along the interfaces is characterized by a scalar interface damage variable. The unilateral contact conditions in the presence of adhesion along the interfaces are given as

$$t^{N(\alpha)} - \left(1 - \omega_{\text{int}}^{(\alpha)}\right) k_N^{(\alpha)} \delta^{N(\alpha)} \leq 0; \quad \delta^{N(\alpha)} \geq 0 \quad (10)$$

$$\left\{ t^{N(\alpha)} - \left(1 - \omega_{\text{int}}^{(\alpha)}\right) k_N^{(\alpha)} \delta^{N(\alpha)} \right\} \delta^{N(\alpha)} = 0 \quad (11)$$

where $t^{N(\alpha)}(\mathbf{x}, t)$ and $\delta^{N(\alpha)}(\mathbf{x}, t)$ are the normal components of the traction and displacement jump vectors, respectively; $\omega_{\text{int}}^{(\alpha)}(\mathbf{x}, t)$ the isotropic, scalar, interface damage variable; and, $k_N^{(\alpha)}$ is the undamaged normal stiffness along the interface. In the tangential direction, adhesion is coupled by a Coulomb type friction model

$$\mathbf{t}^{T(\alpha)} = \mathbf{t}^{Ta(\alpha)} + \mathbf{t}^{Tf(\alpha)} \quad (12)$$

$$\mathbf{t}^{Ta(\alpha)} = \left(1 - \omega_{\text{int}}^{(\alpha)}\right) k_T^{(\alpha)} \boldsymbol{\delta}^{T(\alpha)} \quad (13)$$

$$\left\| \mathbf{t}^{Tf(\alpha)} \right\| \leq t_{\text{crit}}^{(\alpha)} \quad (14)$$

$$\left\| \mathbf{t}^{Tf(\alpha)} \right\| < t_{\text{crit}}^{(\alpha)} \Rightarrow \dot{\boldsymbol{\delta}}^{T(\alpha)} = 0 \quad (15)$$

$$\left\| \mathbf{t}^{Tf(\alpha)} \right\| = t_{\text{crit}}^{(\alpha)} \Rightarrow \dot{\boldsymbol{\delta}}^{T(\alpha)} = \kappa \mathbf{t}^{Tf(\alpha)}, \quad \kappa \geq 0 \quad (16)$$

$$t_{\text{crit}}^{(\alpha)} = \mu_F \left| t^{N(\alpha)} - \left(1 - \omega_{\text{int}}^{(\alpha)}\right) k_N^{(\alpha)} \delta^{N(\alpha)} \right| \quad (17)$$

in which, $\mathbf{t}^{T(\alpha)}(\mathbf{x}, t)$, $\mathbf{t}^{Ta(\alpha)}(\mathbf{x}, t)$ and $\mathbf{t}^{Tf(\alpha)}(\mathbf{x}, t)$ are total, adhesion and friction component of the tangential tractions, respectively; $\hat{\mathbf{t}}^{(\alpha)} = [t^{N(\alpha)}; \mathbf{t}^{T(\alpha)}]$; $\boldsymbol{\delta}^{T(\alpha)}(\mathbf{x}, t)$ is the tangential displacement jump vector; $\hat{\boldsymbol{\delta}}^{(\alpha)} = [\delta^{N(\alpha)}; \boldsymbol{\delta}^{T(\alpha)}]$; and, $k_T^{(\alpha)}$ is the undamaged tangential stiffness along the interface.

2.1 Damage Evolution

The interface damage variable, $\omega_{\text{int}}^{(\alpha)}$, $\alpha = 1, 2, \dots, m$ and phase damage variable, $\omega_{\text{ph}}^{(\eta)}$, $\eta = 1, 2, \dots, n$ represent the inelastic processes within the microstructure. The state of adhesion along the α^{th} partition of the microconstituent interfaces is characterized by the interface damage variable, $\omega_{\text{int}}^{(\alpha)}$, whereas, the nucleation and coalescence of microcracks within the η^{th} partition of the reinforcement and matrix phases are characterized by the phase damage variable, $\omega_{\text{ph}}^{(\eta)}$. In this manuscript, rate-independent and rate-dependent models for the evolution of damage variables are presented. First, the thermodynamics based damage evolution formulation is introduced to model the rate-independent response. Next, the rate-dependent model is described. Rate-dependent response is achieved by a straightforward extension of the rate-independent model using viscoplastic regularization of the Perzyna type. Such rate-dependent damage models with viscoplastic regularization have been proposed for failure characterization of concrete by Simo and Ju [16], Dube *et al.* [17] and others.

2.2 Rate-Independent Damage Model

Let f be the damage potential function in the form

$$f\left(v_{\text{ph}}^{(\eta)}, r_{\text{ph}}^{(\eta)}\right) = \phi\left(v_{\text{ph}}^{(\eta)}\right) - \phi\left(r_{\text{ph}}^{(\eta)}\right) \leq 0 \quad (18)$$

where $v_{\text{ph}}^{(\eta)}(\mathbf{x}, t)$ is phase damage equivalent strain; $r_{\text{ph}}^{(\eta)}(\mathbf{x}, t)$ is damage hardening variable; and ϕ is a monotonically increasing damage evolution function. The evolution equations for damage and hardening variables are given as

$$\dot{\omega}_{\text{ph}}^{(\eta)} = \dot{\lambda} \frac{\partial \phi}{\partial v_{\text{ph}}^{(\eta)}} \quad (19)$$

$$\dot{r}_{\text{ph}}^{(\eta)} = \dot{\lambda} \quad (20)$$

in which, $\dot{\lambda}$ is the consistency parameter for phase damage. Damage accumulation is governed by the Kuhn-Tucker conditions

$$\dot{\lambda} \geq 0; \quad f\left(v_{\text{ph}}^{(\eta)}, r_{\text{ph}}^{(\eta)}\right) \leq 0; \quad \dot{\lambda} f\left(v_{\text{ph}}^{(\eta)}, r_{\text{ph}}^{(\eta)}\right) = 0 \quad (21)$$

The Kuhn-Tucker conditions state that when damage potential function is negative ($f < 0$) rate of damage growth vanish as $\dot{\lambda} = 0$. $\dot{\lambda} > 0$ indicates a damage process where $f = 0$. Neutral loading conditions occur if changes in the strain space do not alter the state of damage equivalent strain ($\dot{\lambda} = 0$ and $f = 0$).

The phase damage equivalent strain is defined as

$$v_{\text{ph}}^{(\eta)} = \sqrt{\frac{1}{2} (\mathbf{F}^{(\eta)} \hat{\boldsymbol{\epsilon}}^{(\eta)})^T \hat{\mathbf{L}}^{(\eta)} (\mathbf{F}^{(\eta)} \hat{\boldsymbol{\epsilon}}^{(\eta)})} \quad (22)$$

where $\hat{\boldsymbol{\epsilon}}^{(\eta)}$ is the vector of principal components of the average strain tensor, $\boldsymbol{\epsilon}^{(\eta)}$, in $\Theta^{(\eta)}$; $\hat{\mathbf{L}}^{(\eta)}$ the tensor of elastic moduli in the principal directions of $\boldsymbol{\epsilon}^{(\eta)}$; and $\mathbf{F}^{(\eta)}(\mathbf{x}, t)$ the weighting matrix. The weighting matrix is introduced to model different damage accumulation characteristics in tensile and compressive loading directions

$$\mathbf{F}^{(\eta)} = \begin{bmatrix} h_1^{(\eta)} & 0 & 0 \\ 0 & h_2^{(\eta)} & 0 \\ 0 & 0 & h_3^{(\eta)} \end{bmatrix} \quad (23)$$

$$h_{\xi}^{(\eta)} = \frac{1}{2} + \frac{1}{\pi} \text{atan} \left[c_1^{(\eta)} \left(\hat{\epsilon}_{\xi}^{(\eta)} - c_2^{(\eta)} \right) \right] \quad (24)$$

where $c_1^{(\eta)}$ and $c_2^{(\eta)}$ represent the contribution of tensile and compressive loadings in the principal directions.

An arctangent damage evolution function is considered for rate-independent characterization of phase damage [4]

$$\phi_{\text{ph}}^{(\eta)} = \frac{\text{atan} \left(a_{\text{ph}}^{(\eta)} \left\langle v_{\text{ph}}^{(\eta)} - v_{0\text{ph}}^{(\eta)} \right\rangle - b_{\text{ph}}^{(\eta)} \right) + \text{atan} \left(b_{\text{ph}}^{(\eta)} \right)}{\pi/2 + \text{atan} \left(b_{\text{ph}}^{(\eta)} \right)} \quad (25)$$

where $v_{0\text{ph}}^{(\eta)}$, is the threshold value of the strain state below which no damage in $\Theta^{(\eta)}$ occurs; $\langle \cdot \rangle = [|\cdot| + (\cdot)]/2$ denotes MacCauley brackets; $a_{\text{ph}}^{(\eta)}$ and $b_{\text{ph}}^{(\eta)}$ are material parameters.

The evolution of rate-independent interface damage variable, $\omega_{\text{int}}^{(\alpha)}$, is described similarly by replacing phase damage equivalent strain and hardening variables with interface damage equivalent strain, $v_{\text{int}}^{(\beta)}(\mathbf{x}, t)$, and interface damage hardening variable, $r_{\text{int}}^{(\beta)}$, in Eq. 18. $v_{\text{int}}^{(\beta)}$ in $S^{(\beta)}$ is expressed in terms of the displacement jump vector as

$$v_{\text{int}}^{(\beta)} = k_N^{(\beta)} \delta^{N(\beta)} + k_T^{(\beta)} \|\boldsymbol{\delta}^{T(\beta)}\| \quad (26)$$

An alternative arctangent law is adopted to model the evolution of interface damage

$$\phi_{\text{int}}^{(\beta)} = \frac{\text{atan}\left(a_{\text{int}}^{(\beta)} v_{\text{int}}^{(\beta)}(\mathbf{x}, t) / b_{\text{int}}^{(\beta)}\right)}{\text{atan}\left(a_{\text{int}}^{(\beta)}\right)}; \quad \phi_{\text{int}}^{(\beta)} \leq 1 \quad (27)$$

in which, $a_{\text{int}}^{(\beta)}$ and $b_{\text{int}}^{(\beta)}$ are material parameters.

2.3 Rate-Dependent Damage Model

Rate dependence of the progressive failure of many composite materials have been well documented and available in open literature (e.g., [18, 19, 20]). At a given strain level, available experimental data suggest that the amount of damage accumulation vary with rate of loading in addition to the possible presence of other effects such as variations in elastic properties [18]. Rate sensitive response of composite materials may be captured by simple modifications of rate-independent models. In this manuscript, the rate-independent damage model presented above is modified using a viscous regularization analogous to Perzyna type [21] in the plasticity theory. The modification for phase damage is achieved by replacing the Kuhn-Tucker conditions (Eq. 21) with the following power law expression of the consistency parameter

$$\dot{\lambda} = \frac{1}{q_{\text{ph}}^{(\eta)}} \left\langle f\left(v_{\text{ph}}^{(\eta)}, r_{\text{ph}}^{(\eta)}\right) \right\rangle^{p_{\text{ph}}^{(\eta)}} \quad (28)$$

where $p_{\text{ph}}^{(\eta)}$ and $q_{\text{ph}}^{(\eta)}$ are rate-dependent phase damage parameters. Modification of the interface damage model is achieved by considering a similar expression for the interface consistency parameter in terms of the rate-dependent interface damage parameters $p_{\text{int}}^{(\beta)}$ and $q_{\text{int}}^{(\beta)}$.

It can be easily shown that regularized rate-dependent damage models converge to rate-independent limit as $q_{\text{ph}}^{(\eta)} \rightarrow 0$ for phase damage and $q_{\text{int}}^{(\beta)} \rightarrow 0$ for interface damage models.

A power law is considered to characterize damage evolution in the rate-dependent model

$$\phi_{\text{ph}}^{(\eta)} = a_{\text{ph}}^{(\eta)} \left\langle v_{\text{ph}}^{(\eta)} - v_{0\text{ph}}^{(\eta)} \right\rangle^{b_{\text{ph}}^{(\eta)}}; \quad \phi_{\text{ph}}^{(\eta)} \leq 1 \quad (29)$$

in which, $a_{\text{ph}}^{(\eta)}$ and $b_{\text{ph}}^{(\eta)}$ are material parameters.

2.4 $(m + n)$ Point Model with Static Partitioning

Equations 8-17 along with the evolution equations for phase and interface damage variables form the nonlinear system of algebraic equations which is evaluated to obtain the eigendeformation fields. The nonlinear system consists of $3m + 6n$ equations for 3-D problems. This

model is therefore referred to as $(m+n)$ point model. m and n denote the number of interface and phase partitions respectively. In phase partitioning, microconstituents are divided into n partitions denoted by $\Theta^{(\eta)}$, $\eta = 1, 2, \dots, n$. The partitioning is conducted such that partitions do not intersect more than one material phase, $\Theta \equiv \bigcup_{\eta=1}^n \Theta^{(\eta)}$ and $\Theta^{(\eta)} \cap \Theta^{(\gamma)} \equiv \emptyset$ for $\eta \neq \gamma$. Microscopically nonlocal inelastic strains, $\boldsymbol{\mu}^{(\gamma)}$, and microscopically nonlocal phase damage variable, $\omega_{\text{ph}}^{(\eta)}$ are associated with partition $\Theta^{(\eta)}$. In interface partitioning, microstructural interfaces are divided into m partitions and corresponding interface partition domain is denoted by $S^{(\alpha)}$, $\alpha = 1, 2, \dots, m$. In contrast to the phase partitioning, interface partitions overlap to satisfy continuity of the displacement field along the interface; and $S \equiv \bigcup_{\alpha=1}^m S^{(\alpha)}$. Displacement jumps, $\hat{\boldsymbol{\delta}}^{(\alpha)}$, and interface damage variable $\omega_{\text{int}}^{(\alpha)}$ are associated with interface partition, $S^{(\alpha)}$.

The accuracy and efficiency of the $(m+n)$ point models is directly related to the partitioning of the microstructural domain constituents. Clearly, selecting large values for phase and interface partitions increase the level of accuracy accompanied by an increase in the computational cost. A sequence of $(m+n)$ point models may therefore be constructed, where the most efficient member represents simultaneous failure at all material points within each microconstituent and interface. For instance, the most efficient model for a 2-phase fibrous composite system has two phase partitions ($n = 2$, reinforcement and matrix) and a single interface partition ($m = 1$). A-priori knowledge that certain microconstituents or interface do not fail will further reduce the computational cost. The $(0+1)$ point model may also be chosen if interface and fiber is assumed damage-free. The most comprehensive member of the sequence coincides with the direct homogenization method, in which failure is evaluated separately at each finite element of the microstructural mesh (i.e., $n = n_{\text{el}}$ and $m = m_{\text{el}}$ where n_{el} and m_{el} are the number of phase and interface elements within the microstructural mesh).

Static and dynamic strategies have been previously proposed for partitioning of the microstructural geometry [1]. In static domain partitioning (SDP) strategy, model order (m and n) and division of the microstructural phases and interfaces into $\Theta^{(\eta)}$, $\eta = 1, 2, \dots, n$ and $S^{(\alpha)}$, $\alpha = 1, 2, \dots, m$, respectively, are conducted prior to the analysis of the macroscale problem. In dynamic domain partitioning (DDP) strategy, the microstructural domain is repartitioned based on the evolution of the material failure as the macroscopic analysis progresses. DDP strategy is advantageous when preprocessing cost is substantially lower than the cost of non-linear iterations. Otherwise, SDP strategy with higher order $(m+n)$ point model may be more efficient and accurate. The SDP strategy is adopted in this manuscript.

The static domain partitioning strategy is illustrated in Fig. 2. For a given model order m and n , microstructural phases and interfaces are partitioned based on the elastic macroscopic strains $\bar{\boldsymbol{\epsilon}}^{\text{el}}$ which is computed in the preliminary linear analysis of the macroscopic problem. The corresponding microstructural deformation is obtained as $\boldsymbol{\epsilon}^{\text{el}} = \mathcal{G}\bar{\boldsymbol{\epsilon}}^{\text{el}}$. \mathcal{G} is the elastic polarization function in the matrix form. The microstructural domain, Θ , and interface, S is partitioned into $\Theta^{(\eta)}$, $\eta = 1, 2, \dots, n$ and $S^{(\alpha)}$, $\alpha = 1, 2, \dots, m$, respectively based on the amplitude of the microscopic stress and interface traction values. Coefficient tensors are then computed for phase and interface damage partitions in the preprocessing stage and remain constant throughout the macroscopic analysis. For a comprehensive treatment of the static partitioning strategy, we refer to Ref. [1].

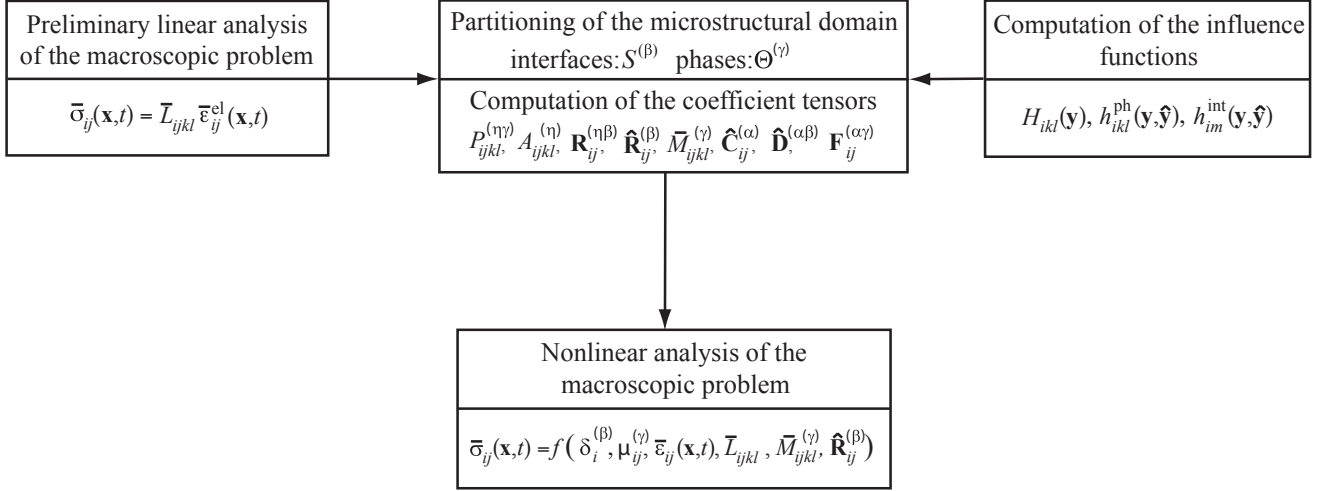


Figure 2: Static Domain Partitioning (SDP).

3 Validation Strategy

The $(m + n)$ point model with static domain partitioning has been previously verified against direct homogenization method [1]. The $(m + n)$ point model was shown to provide computational cost savings of 3 orders of magnitude without significantly compromising on accuracy compared to the direct homogenization method. In this manuscript, we focus on a systematic calibration and validation of the $(m + n)$ point models.

Validation of multiscale computational models present unique challenges compared to a single scale phenomenological model. For example, whereas the validation of phenomenological models commonly involve calibration of model parameters with experiments designed to uniquely identify a single model parameter at a time, such a methodology cannot be extended to calibrate models developed using multiscale methods. In multiscale modeling, model parameters are commonly associated with microstructural constituents. Most experimental methods provide observations at macroscopic scale, and therefore, may not be used to uniquely identify multiscale model parameters one at a time. Despite current developments in experimentation technologies which allow estimation of few microscopic parameters directly (e.g., [22]), it is essential to develop novel validation strategies specifically suited for multiscale models.

The model validation methodology described below introduces the concept of repository of experiment simulator modules, which has been implemented to validate the $(m + n)$ point models against experimental data. The validation methodology is generic in the sense that it may be implemented without extensive effort to assess the validity of alternative hierarchical multiscale models [23].

Validation of the $(m + n)$ point models are conducted in two steps:

1. Calibration of the multiscale parameters using a suite of experiments.
2. Simulation of a complex system using the calibrated model and assessment of the model by comparing the simulation predictions with experimental results. Calibration and validation simulations must be dissimilar for proper validation of the model.

Figure 3 illustrates the algorithm of the calibration methodology for the $(m + n)$ point model. The calibration is conducted in three steps:

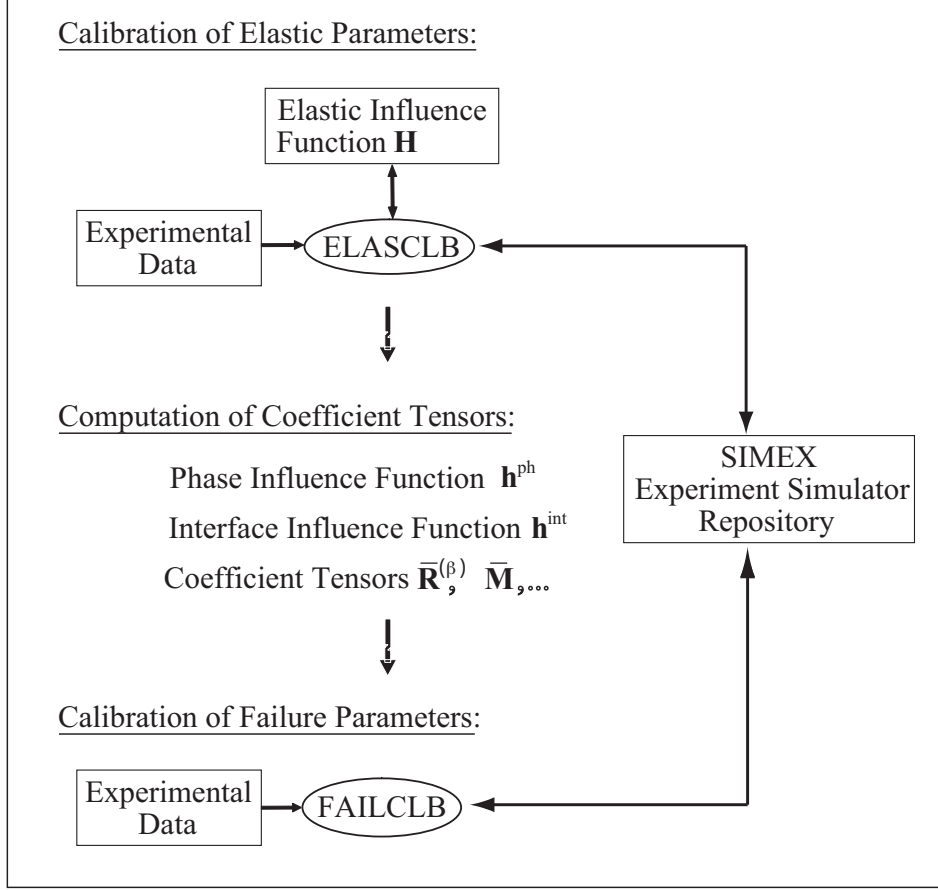


Figure 3: Calibration Algorithm.

1. Calibration of the elastic parameters;
2. Computation of coefficient tensors;
3. Calibration of the phase and interface failure parameters.

Elastic and failure parameter calibrations are conducted using programs ELASCLB and FAILCLB, respectively. ELASCLB and FAILCLB, collectively called MNCLB, are optimization algorithms to minimize the discrepancy between the experimental and simulation predictions as described below.

In the context of the static partitioning strategy, the calibration of elastic and failure parameters, in addition to computation of the coefficient tensors is conducted prior to the macroscopic analysis. In the first step of the calibration algorithm, ELASCLB is employed to evaluate the optimal elastic material parameters. The elastic influence function, \mathbf{H} , which is a function of the elastic material parameters, is updated at every step of the optimization. The phase and interface damage influence functions (\mathbf{h}^{ph} and \mathbf{h}^{int} , respectively) are computed following the elastic calibration step. The influence functions \mathbf{H} , \mathbf{h}^{ph} and \mathbf{h}^{int} are solutions to influence function problems stated in the Appendix. The final step employs FAILCLB which evaluates the optimal failure parameters by minimizing the discrepancy between experimental data and numerical simulation predictions. An experiment simulator repository (SIMEX) is devised to conduct numerical simulations at every step of the optimizations in MNCLB. SIMEX is composed of a collection of experiment simulator modules as illustrated in Fig. 4.

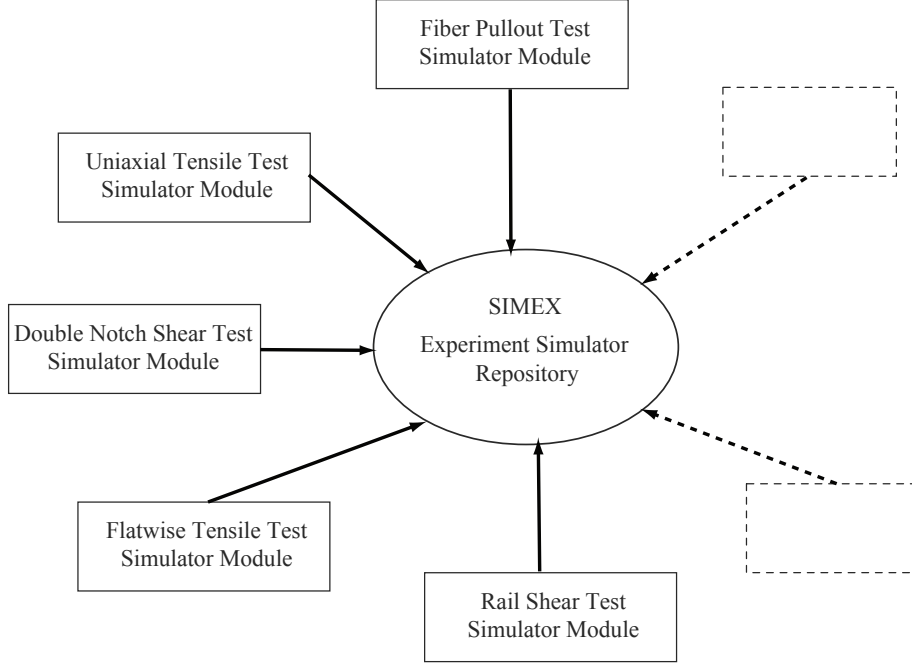


Figure 4: Experiment Simulator Repository.

SIMEX architecture permits incorporation of additional experiment simulators without altering the structure of the optimization program. Such architecture is particularly powerful for calibration of multiscale models in which a multitude of parameters are identified simultaneously based on experimental data at various scales.

The calibration code communicates with a commercial finite element software (Abaqus) to conduct numerical simulations along with appropriate user supplied subroutines. The structure of the calibration code implementation is shown in Fig. 5. The objective function is constructed based on experimental data and SIMEX simulation predictions as described below. The communication with the finite element software is conducted in SIMEX.

3.1 Optimization Algorithm

A model, $\mathcal{M}(\mathbf{x})$, is said to be calibrated when the model parameter set, \mathbf{x} , minimizes the objective function

$$\mathbf{x}^* = \arg \min_{\mathbf{x} \in \mathbb{R}^b} \frac{1}{2} \mathbf{F}(\mathbf{x})^T \mathbf{F}(\mathbf{x}) = \frac{1}{2} \sum_{i=1}^a [e_i - s_i(\mathbf{x})]^2 \quad (30)$$

subject to $\mathbf{l} \leq \mathbf{x} \leq \mathbf{u}$

in which, \mathbf{x}^* is the calibrated material parameter set, \mathbf{e} the data provided by the experiments; $\mathbf{s}(\mathbf{x})$ is the simulation predictions of model, $\mathcal{M}(\mathbf{x})$; $\mathbf{F}(\mathbf{x}) = \mathbf{e} - \mathbf{s}(\mathbf{x})$; b and a the lengths of the model parameter set, \mathbf{x} , and data set, \mathbf{e} , respectively; and \mathbf{l} and \mathbf{u} are the lower and upper bound vectors for the model parameter set.

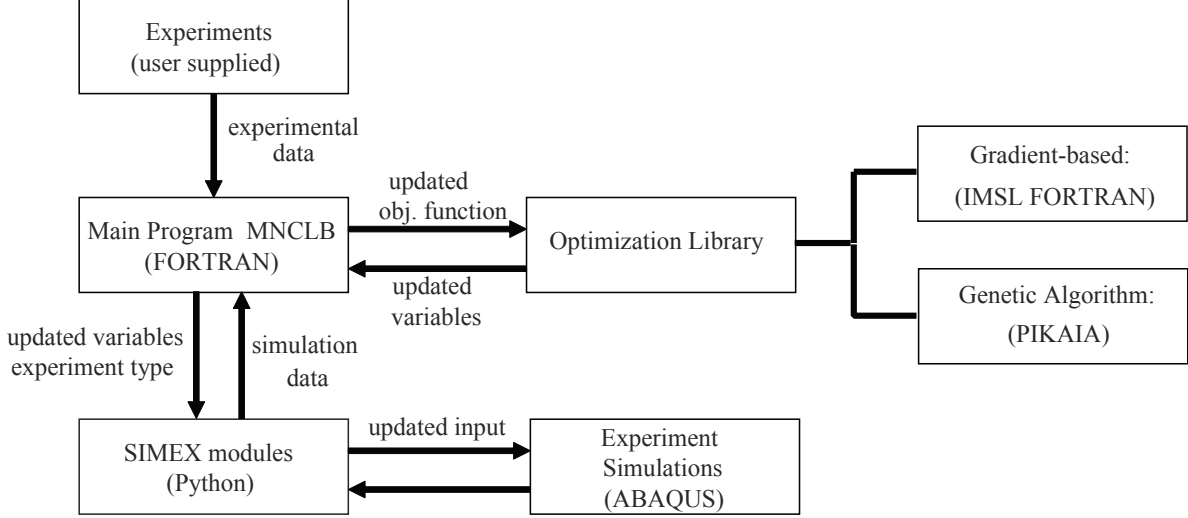


Figure 5: Structure of the calibration code.

3.1.1 Gradient-based optimization

The optimization problem stated in Eq. 30 is evaluated using the Levenberg-Marquardt algorithm with active set strategy to impose simple bounds on the model parameters. IMSL Fortran Library Routine (DBCLSF) is employed. Levenberg-Marquardt algorithm is based on the trust region approach [24]. The model parameter set at each iteration is updated by

$$\bar{\mathbf{x}}^{k+1} = \bar{\mathbf{x}}^k - (\bar{\mathbf{J}}^T \bar{\mathbf{J}} + \mu \mathbf{I})^{-1} \bar{\mathbf{J}}^T \bar{\mathbf{F}} \quad (31)$$

in which, $\bar{\mathbf{F}}$ includes components of \mathbf{F} for which the model parameters lie inside bounds (i.e., $i = 1, 2, \dots, b$ such that $l_i < x_i < u_i$); $\bar{\mathbf{J}}$ the jacobian of $\bar{\mathbf{F}}$; μ the Levenberg-Marquardt parameter to ensure that iterates lie within a trust region δ (i.e., $\mu = 0$ if $\|\bar{\mathbf{J}}^{-1} \bar{\mathbf{F}}\|_2 = \delta$ and $\mu > 0$ otherwise); \mathbf{I} the identity matrix; and superscripts indicate optimization iteration count. A finite difference scheme is employed to approximate the jacobian. μ and δ is computed based on a locally constrained hook step algorithm [25]. The optimality conditions for termination of optimizations are given as [26]

$$\|g(x_i)\| \leq \text{tol}; \quad \text{if } l_i < x_i < u_i \quad (32)$$

$$g(x_i) < 0; \quad \text{if } x_i = u_i \quad (33)$$

$$g(x_i) > 0; \quad \text{if } x_i = l_i \quad (34)$$

where $\mathbf{g} = \bar{\mathbf{J}}^T \bar{\mathbf{F}}$. The components of $\bar{\mathbf{F}}$ are updated based the active set strategy as model parameters reach the bounds or optimality conditions are violated [27].

3.1.2 Evolutionary optimization

Evolutionary algorithms provide an alternative approach to the optimization problem. This approach is based on the observation that a march towards an extremum of an objective function resembles the evolution of living organisms into superior individuals. The primary driving mechanism of evolution of biological systems, i.e., natural selection, is therefore employed to

evaluate the optimization problem. Literature on evolutionary algorithms is vast and evolutionary techniques have been employed to evaluate a wide range of problems (e.g., [11, 12]). In this study, a genetic algorithm is used to evaluate the calibrated material set \mathbf{x}^* . A public domain genetic algorithm software, PIKAIA [28], is incorporated into the SIMEX framework.

Genetic algorithms typically consist of the creation of a population of individuals, and execution of a set of rules to breed subsequent generations of the population until one individual reaches the desired fitness value. An individual is defined as a point in the material parameter space

$$\hat{\mathbf{x}} \in \mathcal{B}; \quad \mathcal{B} = \left\{ \mathbf{x} \in \mathbb{R}^b \mid \mathbf{l} \leq \mathbf{x} \leq \mathbf{u} \right\} \quad (35)$$

The population is defined as a set of n_{pop} individuals. Initial population of individuals are selected by randomly sampling the parameter space \mathcal{B} . The fitness of an individual is proportional to the distance to the calibrated material parameter set, \mathbf{x}^*

$$\mathcal{F}(\hat{\mathbf{x}}) = \frac{C}{\mathbf{F}(\hat{\mathbf{x}})^T \mathbf{F}(\hat{\mathbf{x}})} \quad (36)$$

where, C is a constant algorithmic scaling parameter. Subsequent generations of the population are created using the following strategy:

- a. selection of parents from the current population;
- b. cross-over and mutation operations to generate offsprings; and
- c. generational replacement using elitism.

Parents are selected among the individuals within the population using a roulette wheel algorithm. The probability of selection of an individual in the population is evaluated by the relative fitness function:

$$\mathcal{F}'(\hat{\mathbf{x}}) = (f_d + 1)(n_{\text{pop}} + 1) - 2r(\mathcal{F})f_d \quad (37)$$

in which $0 \leq f_d \leq 1$ is an algorithmic parameter which controls the sensitivity of the relative fitness function to rank, $r \in \{1, n_{\text{pop}}\}$, such that $r = n_{\text{pop}}$ and $r = 1$ are the least fit and fittest individuals, respectively.

Cross-over operation is used to breed two offsprings from two parents selected using the roulette wheel algorithm. This operation, illustrated in Fig. 6, is conducted using the denary representation (chromosome) of the individuals. The chromosomes of the parents are split into two parts at a randomly selected locus. The chromosome fragments to the right of the split are interchanged and concatenated to the left part to form the offsprings. The offsprings are then randomly mutated. The mutation operation consists of replacing a targeted gene (a digit in the denary representation of the individual) in the chromosome offspring with a randomly created gene. The mutation operation increases the probability of avoiding convergence to a local minimum.

A generational replacement algorithm with elitism is employed to breed new generations of individuals. In this study, the population is kept constant throughout generations. The algorithm consists of creating n_{pop} offsprings which constitutes the candidates for the next generation of individuals. The fittest individual of the new and the previous generation is artificially added to the new population (elitism) to eliminate the possibility of losing fittest individuals in the cross-over and mutation operations.

While the genetic algorithm strategy defined above has been successfully applied to evaluate the global minima of many complex problems, the solution is trapped to local minima in

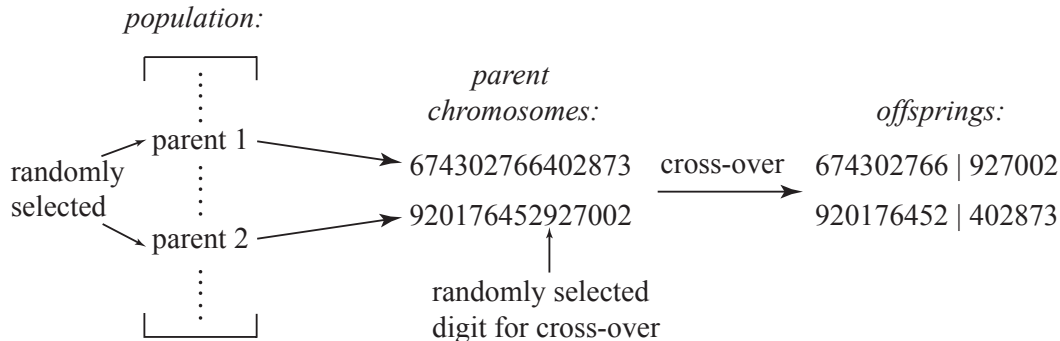


Figure 6: Illustration of the cross-over operation to breed offsprings from parent chromosomes in the genetic algorithm.

others[29]. A detailed study of the characteristics of a number of evolutionary algorithms for finding global minima with real valued parameters are described in [30]. In this study genetic algorithm is invoked multiple times to increase the reliability of the computed optimal parameters.

4 Validation Examples

The capabilities of the $(m + n)$ point model and the validation strategy are demonstrated considering two composite systems: (i) ceramic matrix composite (CMC) system; and (ii) polymer matrix composite system.

4.1 Ceramic Matrix Composites

We consider a silicon carbide fiber-reinforced silicon carbide matrix composite. The composite system consists of high quality Hi-Nicalon type S fibers and matrix material processed by melt-infiltration. Such high quality CMC systems are often being used in aircraft jet engine [31] and gas turbine [32, 33] components.

Calibration of the $(m + n)$ point models are conducted using specimens with $[0/90]_{2s}$ laminate. A thin matrix layer with approximately 1/3 of the ply thickness exists between each composite ply as shown in Fig. 7. Experiments conducted on the composite laminates consists of (a) flatwise tensile (ASTM-C-297); (b) double notch shear (ASTM-D-3846-94); and (c) uniaxial tensile tests. Flatwise tensile tests were conducted on flat round shaped specimens to measure the interlaminar strength of the composite system. The failure was observed primarily within the thin matrix interlayer. Double notch shear tests were conducted to quantify the macroscopic shear strength of the composite specimens. Uniaxial tensile testing was conducted in the fiber direction only. Experimental results and numerical predictions of the present composite system are export controlled. We present normalized results with randomly selected normalization constants only.

The optimization-based calibration scheme is used to identify the microscopic phase and interface parameters of the $(m + n)$ point models. 0^0 and 90^0 layers are modeled using a fibrous unit cell. The finite element mesh of the unit cell is provided in Fig. 8. The $(0 + 2)$ and $(1 + 2)$ point models are chosen to idealize the unit cell response, where one point is

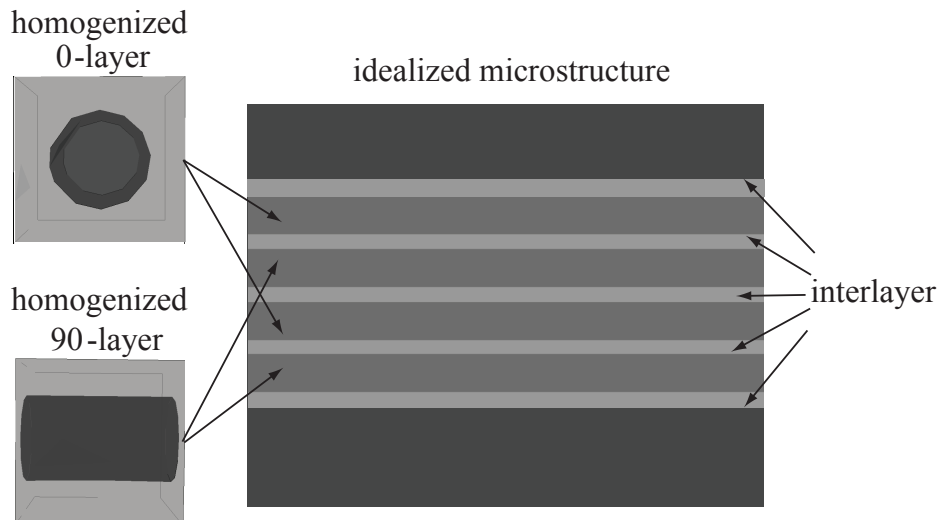


Figure 7: Idealized meso- and micro-structure of the laminated CMC composite.

reserved for each of the two phases (matrix and fiber). Perfect interface and one point interface damage representations are chosen for the former and latter models, respectively. Fiber and matrix materials are assumed to be isotropic. The interlayer is modeled explicitly assuming transversely isotropic response. The thickness direction is taken to be the axis of transverse isotropy. The evolution of the matrix, fiber and interface damage is modeled using the rate-independent damage model (Section 2.2) with the arctangent evolution laws (Eqs. 25,27).

The response of the laminated composite system is defined using 19 phase and 5 interface material parameters in the microscale. The available experimental data does not provide sufficient information for the calibration of all 19 parameters for (0 + 2) and 24 parameters for (1 + 2) point models. The number of independent parameters is reduced by the following idealizations:

- a. Poisson's ratios of the matrix and fiber material are assumed to be the same ($\nu_M = \nu_F$);
- b. The elastic and failure properties of the interlayer are assumed to be identical to the matrix material along directions perpendicular to the axis of transverse isotropy (i.e., $E_{I1} = E_M$, $\nu_{I13} = \nu_{I12} = \nu_M$). The only variation between the interlayer and matrix material is the initial elastic modulus in the direction of transverse isotropy which is assumed to have significant initial damage.
- c. Weighting matrix parameters for the matrix and fiber materials are not calibrated since experiments on the compressive response of the composite laminate are not available.
- d. Threshold values for damage accumulation are set to zero. Therefore, damage is assumed to accumulate from the onset of loading ($v_{0ph}^{(M)} = v_{0ph}^{(F)} = 0$).
- e. Initial interface stiffness in the normal and tangential directions are assumed to be the same ($k_N = k_T$).
- f. Post-debonding interface friction is ignored ($\mu_F = 0$)

The microscopic material parameters to be calibrated are reduced to 9 phase (E_F , E_M , ν_F , E_{I3} , G_{I13} , $a_{ph}^{(F)}$, $b_{ph}^{(F)}$, $a_{ph}^{(M)}$, $b_{ph}^{(M)}$), and 3 interface (a_{int} , b_{int} , k_N) parameters. The matrix and fiber phase elastic parameters (E_F , E_M and ν_F) are identified in the elastic calibration

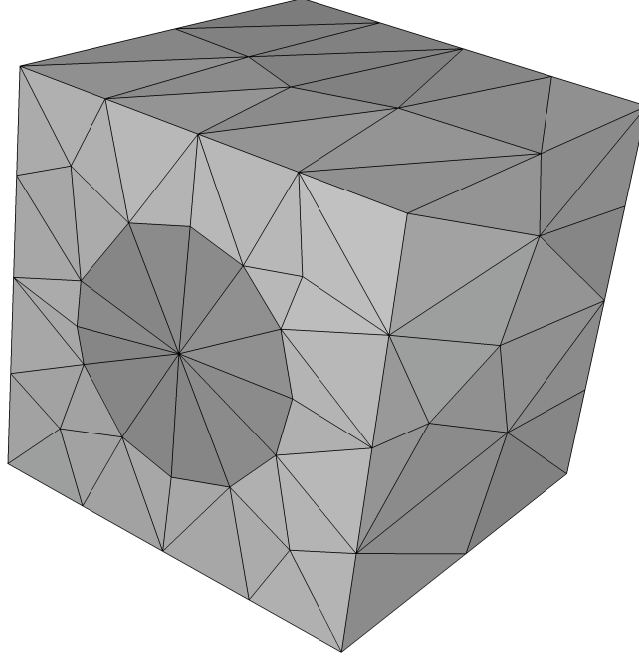


Figure 8: Fibrous microstructure mesh for the 0 and 90 layers.

step (see Section 3). The elastic properties describing the response in the transverse direction of the interlayer (E_{I3} and G_{I13}) are identified in the failure parameter calibration step since direct experimental data in the elastic regime were not available. The elastic modulus of Hi-Nicalon type S fiber is documented in the open literature. In this analysis, the elastic modulus of the fiber material at room temperature is taken to be 420GPa as provided by Ref. [34]. The standard deviation in the elasticity modulus is less than 2.5%. The Poisson's ratio of the composite system is provided by the uniaxial tensile tests. Elastic modulus of the matrix material is identified using ELASCLB program based on the elastic data provided by uniaxial tensile tests. Using the calibrated microscopic material parameters, the simulated elastic modulus of the laminated composite system is within 99% of the experiments.

Program FAILCLB is used to identify the remaining parameters (E_{I3} , G_{I13} , $a_{\text{ph}^{(F)}}$, $b_{\text{ph}^{(F)}}$, $a_{\text{ph}^{(M)}}$, $b_{\text{ph}^{(M)}}$ for (0+2) and (1+2) point models, in addition to a_{int} , b_{int} , k_N for (1+2) point model) in the failure parameter calibration step. The interlaminar and shear strength from the flatwise tensile and double notch shear tests in addition to stress-strain curves from the uniaxial tensile tests are simultaneously used to calibrate the failure parameters. Finite element discretization of the flatwise tensile, double notch shear and uniaxial tensile test specimens are shown in Fig. 9.

The simulated and experimental normalized stress-strain curves for the uniaxial tensile test is shown in Fig. 11. Simulations using the calibrated model estimates the uniaxial tensile strength with 4% error compared to mean strength (standard deviation is 4.5% of the mean). Strength in the transverse direction using the calibrated model is within 5% of the mean strength (8.5% standard deviation) observed in flatwise tensile tests. Simulation of the double notch shear test shear strength within 93% of the experimental value. Figure 11 indicates a marginal improvement in the calibrated model response when interface damage effects are present. This suggest that failure largely initiates within the matrix material.

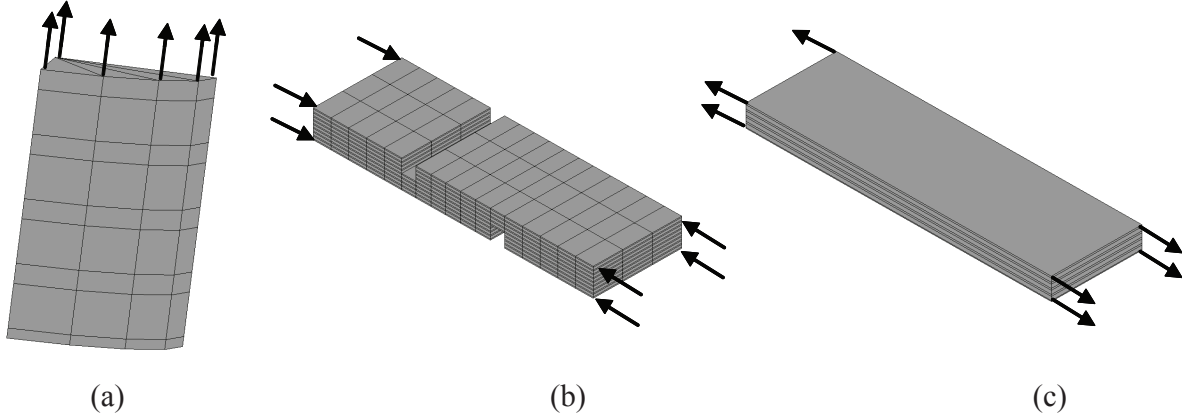


Figure 9: Finite element discretization of the flatwise tensile, double notch shear and uniaxial tensile test specimens used in the calibration of the laminated CMC composite.

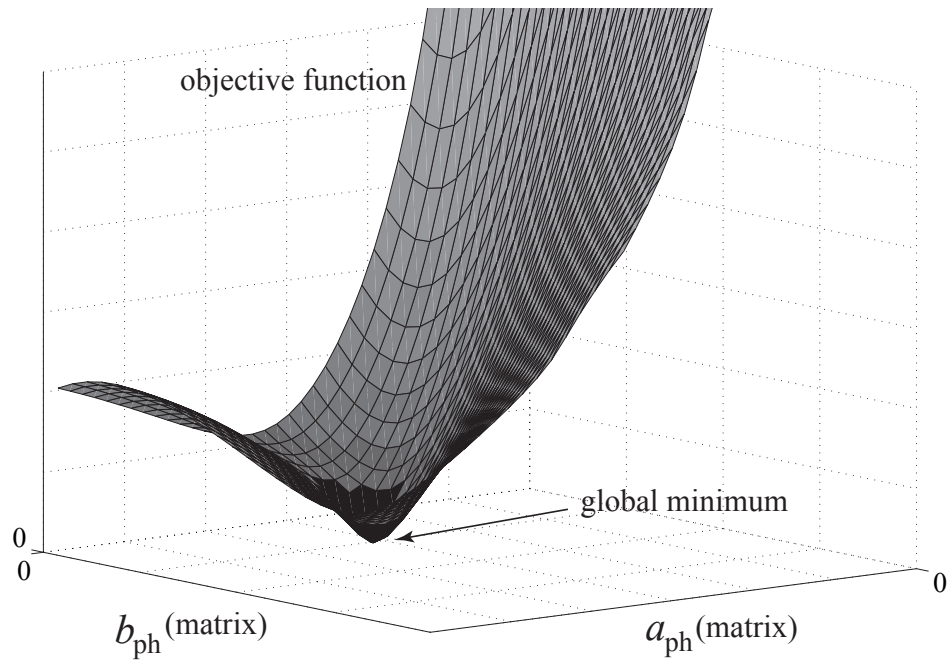
Remark: The calibration of the material parameters for $(0 + 2)$ and $(1 + 2)$ point models were conducted using gradient-based and genetic algorithms. Global convergence in the gradient based algorithm is achieved by multiple parallel evaluations with random initial parameter configurations. The projection of the multi-dimensional objective function onto $a_{\text{ph}^{(F)}} - b_{\text{ph}^{(F)}}$ and $a_{\text{ph}^{(M)}} - b_{\text{ph}^{(M)}}$ subspaces are shown in Fig. 10. The figures show a rather smooth variation of the objective function within the subspaces. Smoothness of the objective function is essential for the performance and validity of the gradient-based optimization methods. Genetic algorithms, while tailored to finding the global minimum, tend to converge to local minima [30] even when advanced modifications to the algorithm is employed. Similar to the gradient based approach, genetic algorithm is evaluated repeatedly to increase the reliability of the global optimal set of parameters. Gradient-based and genetic algorithms yield nearly identical optimal parameter set for the present problem.

4.2 Polymer Matrix Composites

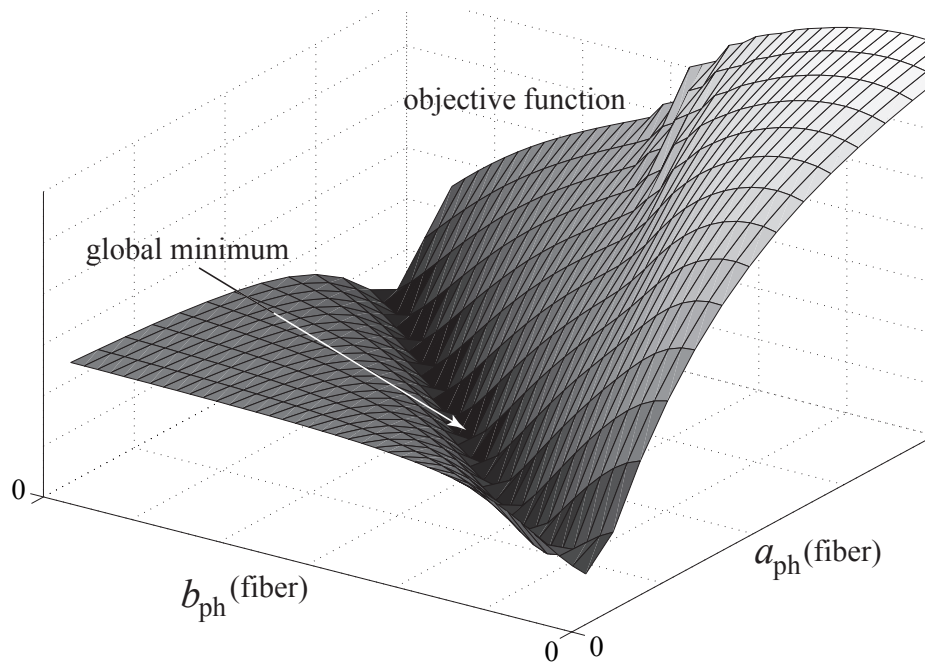
In this section, rate-dependent nonlinear behavior of a glass fiber composite system is investigated. The composite system consists of S2-glass fibers and an epoxy (8553-40) matrix material. The $(m + n)$ point model is calibrated using unidirectional off-axis coupon specimens loaded at various strain rates. The calibrated $(m + n)$ point model is then validated by predicting the rate-dependent response of laminated systems.

Thiruppukuzhi and Sun [35] conducted a suite of uniaxial tensile tests on S2-glass/epoxy composite systems. The nominal resin content is reported as 35%. Off-axis specimens with cut angles of 15^0 , 30^0 , 45^0 , 60^0 and 90^0 were loaded at strain rates of 0.0001/s, 0.01/s and 1/s up to failure. Experimental findings reported in [35] are employed to calibrate the model parameters of a $(0 + 2)$ point model. Each microphase (fiber and matrix) is modeled using a single point. Perfect bonding is assumed along the interface ($m = 0$). Matrix and fiber phases consist of isotropic materials with damage. Rate-dependent effects were considered by utilizing the rate-dependent damage model described in Section 2.3. Damage evolution is described by the power law (Eq. 29).

The response of the composite system is fully defined using 18 microscopic material parameters. The weighting parameters for the matrix ($c_1^{(M)}$ and $c_2^{(M)}$) and fiber materials ($c_1^{(F)}$



(a)



(b)

Figure 10: The variation of the objective function in the parameter subspaces: (a) matrix damage parameter subspace; (b) fiber damage parameter subspace.

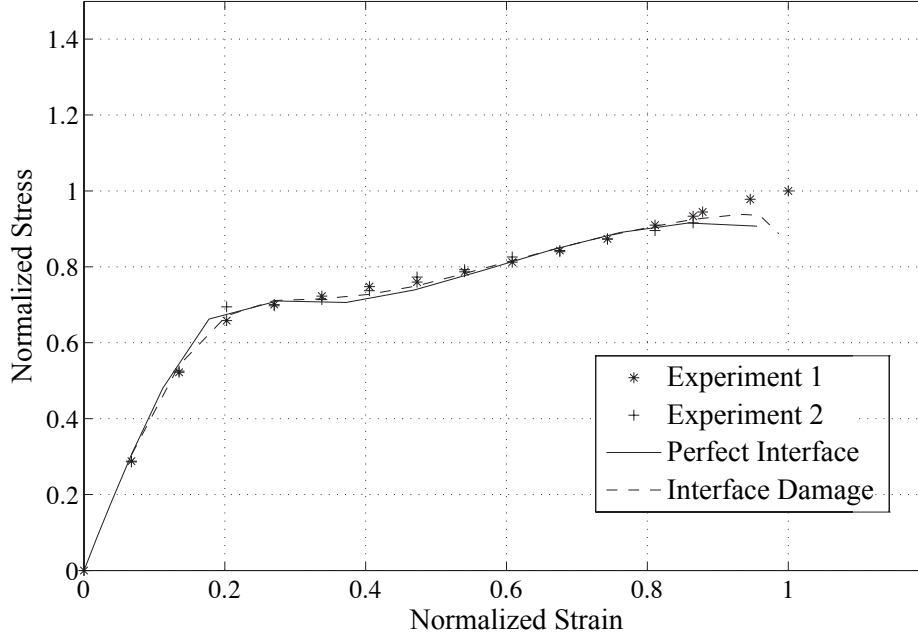


Figure 11: Simulated and experimental uniaxial tensile stress strain curves at room temperature.

and $c_2^{(F)}$) are not calibrated since experiments on the compressive response are not available. Threshold values for damage accumulation are set to zero. Therefore, damage is assumed to accumulate from the onset of loading ($v_{0ph}^{(M)} = v_{0ph}^{(F)} = 0$). Calibration of the matrix (E_M and ν_M) and fiber (E_F and ν_F) elastic parameters is carried out in the elastic parameter calibration step using ELASCLB program. The virgin elastic modulus of the S2-glass fiber [36] is used as the in-situ elastic fiber modulus $E_F = 87.5\text{GPa}$. The Poisson ratio of the microconstituents is set to the Poisson ratio of the overall unidirectional composite system $\nu_M = \nu_F = 0.29$ provided in [35]. The elastic modulus of the matrix material is calibrated using ELASCLB. The calibration yields $E_M = 4.775\text{GPa}$.

The failure parameters of the (0 + 2) point model were calibrated using experiments on 15° and 30° off-axis specimens. Loading with slow (0.0001/s), medium (0.01/s), and fast (1/s) strain rates were applied to each geometric configuration. Program FAILCLB is employed to conduct the calibrations. Gradient-based and genetic algorithms are utilized in the calibration of the model. Figures 12 and 13 illustrate the fitted stress-strain curves for the 15° and 30° off-axis specimens, respectively, for slow, medium and fast strain rates in addition to two calibration approaches. The difference between the predictions of the gradient-based and genetically optimized models are insignificant. Tensile strength of 15° and 30° off-axis specimens were simulated within 92-99% accuracy, whereas the strains-to-failure were within 87.5-99% of the experimental results for all the tested specimens. Tensile strength and strain-to-failure values are summarized in Table 1.

The simulated and experimental stress strain response of 45° , 60° , and 90° off-axis unidirectional specimens subjected to slow strain rates are shown in Fig. 14 in addition to 15° and 30° specimen curves which were used in the calibration step. A good agreement is observed between the predicted and experimental curves. 45° , 60° , and 90° stress-strain curves were not used in the calibration of the model parameters and constitute a preliminary validation step.

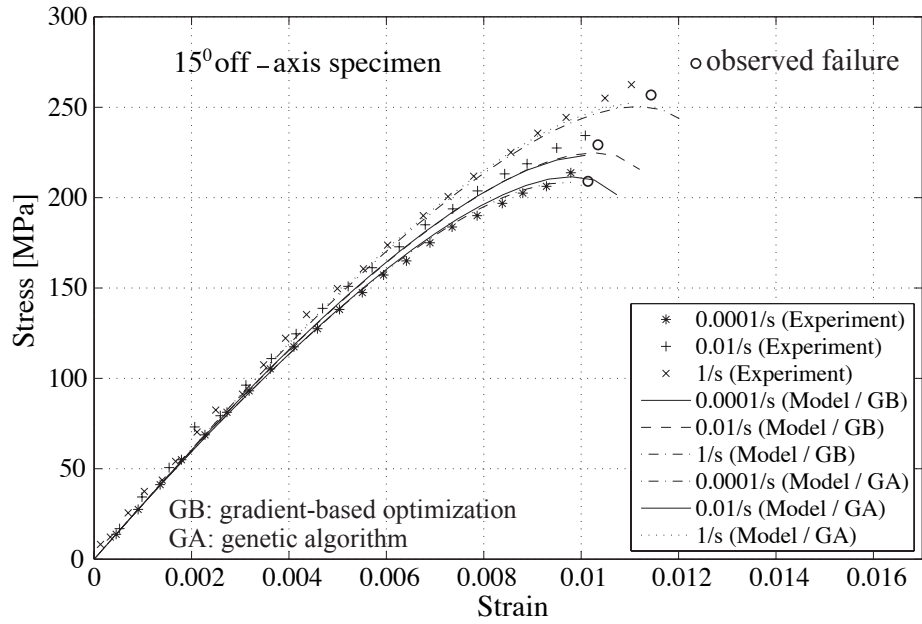


Figure 12: Simulated and experimental uniaxial tensile stress strain curves for the 15° off-axis specimen at various strain rates.

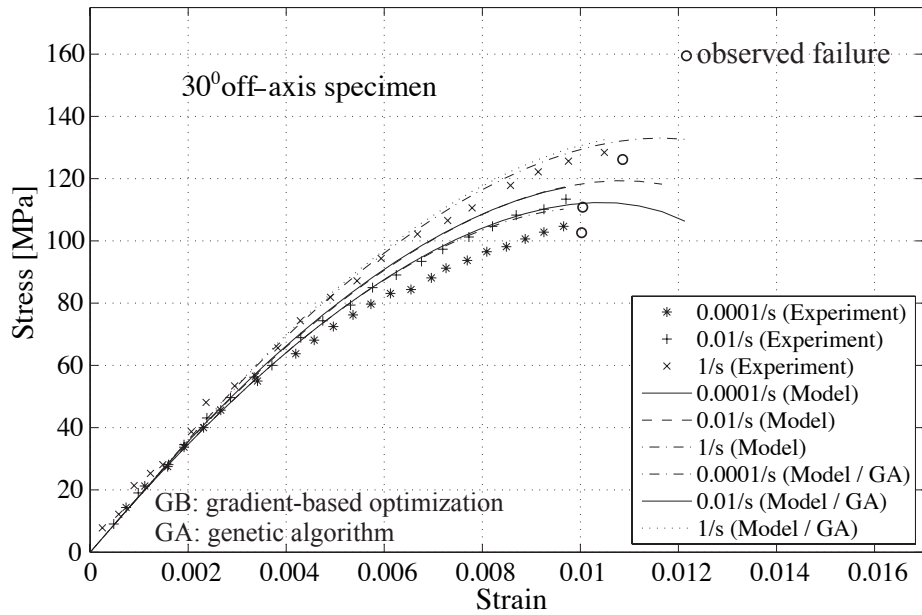


Figure 13: Simulated and experimental uniaxial tensile stress strain curves for the 30° off-axis specimen at various strain rates.

Table 1: Strength and strains-to-failure for the 15° and 30° off-axis specimens at various strain rates.

		15° off-axis			30° off-axis		
		0.0001/s	0.01/s	1/s	0.0001/s	0.01/s	1/s
strength [MPa]	simulation	211	225	250	112	119	133
	experiment	213	234	262	104	113	128
strain-to-failure [%]	simulation	0.98	1.02	1.11	1.02	1.07	1.17
	experiment	0.97	1.01	1.1	1.02	0.97	1.04

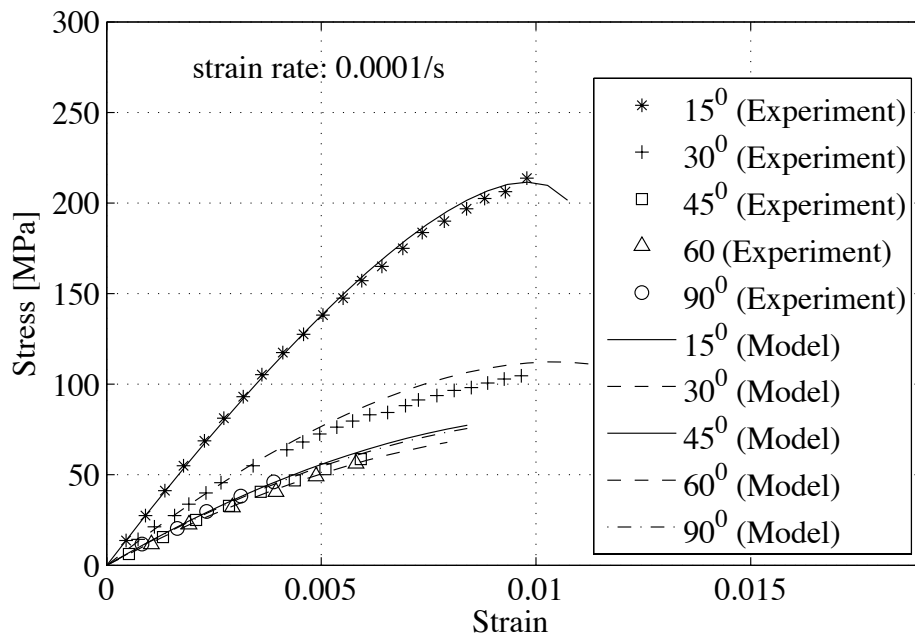


Figure 14: Simulated and experimental uniaxial tensile stress strain curves for the 15° , 30° , 45° , 60° , and 90° off-axis specimens at 0.0001/s strain rate.

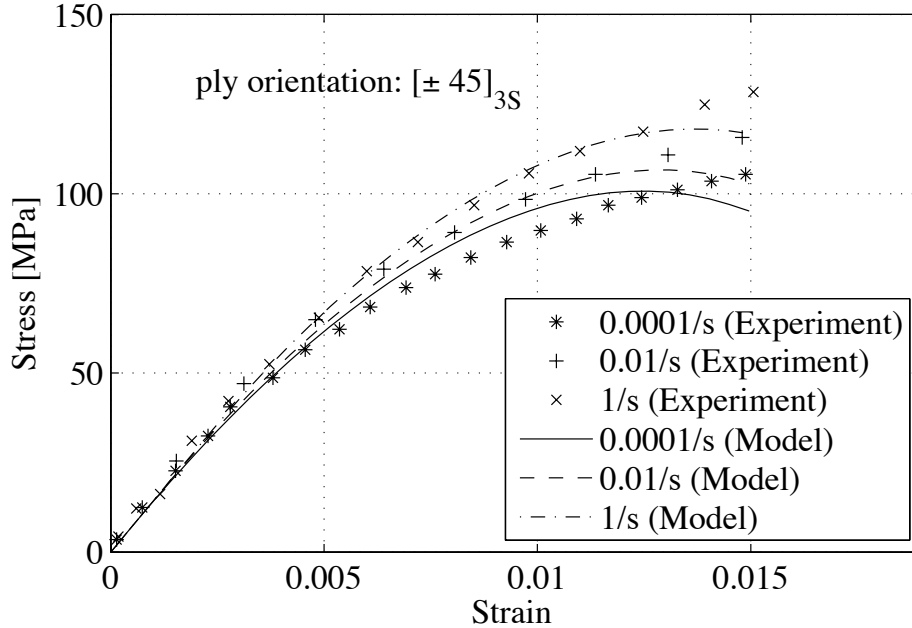


Figure 15: Simulated and experimental uniaxial tensile stress strain curves for the $[\pm 45]_{3S}$ S2-glass laminate at various strain rates.

The calibrated (0 + 2) point model was then used to predict the response of laminated composite systems composed of S2-glass fibers and epoxy matrix for two symmetric laminate constructions. The constructions are a balanced $[\pm 45]_{3S}$ and an unbalanced $[+15/ - 75]_{3S}$ laminate system. The symmetric laminates have 12 plies each. Figures 15 and 16 illustrate the model predictions with the experimental stress-strain curves for slow (0.0001/s), medium (0.01/s), and fast (1/s) strain rates. A reasonable agreement was observed between the model predictions and the experimental results. Maximum stresses for the given strain range were predicted to be within 92-96% accuracy for the balanced $[\pm 45]_{3S}$ systems and 85-92% accuracy for the unbalanced $[+15/ - 75]_{3S}$ composite system.

5 Conclusions

The manuscript presents an optimization-based calibration model strategy for computational homogenization methods. The method features an experimental simulator repository, which is used to simulate experiments for model calibration. The optimization-based approach provides the best possible fit of model parameters to minimize the error between simulations and experimental observations for all tests. The method has been fully integrated within a commercial finite element software (Abaqus). Several important challenges and questions remain in validation and calibration of the mathematical homogenization based multiscale models. First issue is the determination of the type and number of calibration experiments. At the present time, the choice of experiments is very limited and depends on what is available rather than what is needed. Sensitivity studies of identified material parameters present additional challenges. While the complexity of the multiscale models prohibits analytical or semi-analytical sensitivity studies, a rigorous parametric study is critical to increase the confidence in multiscale model predictions.

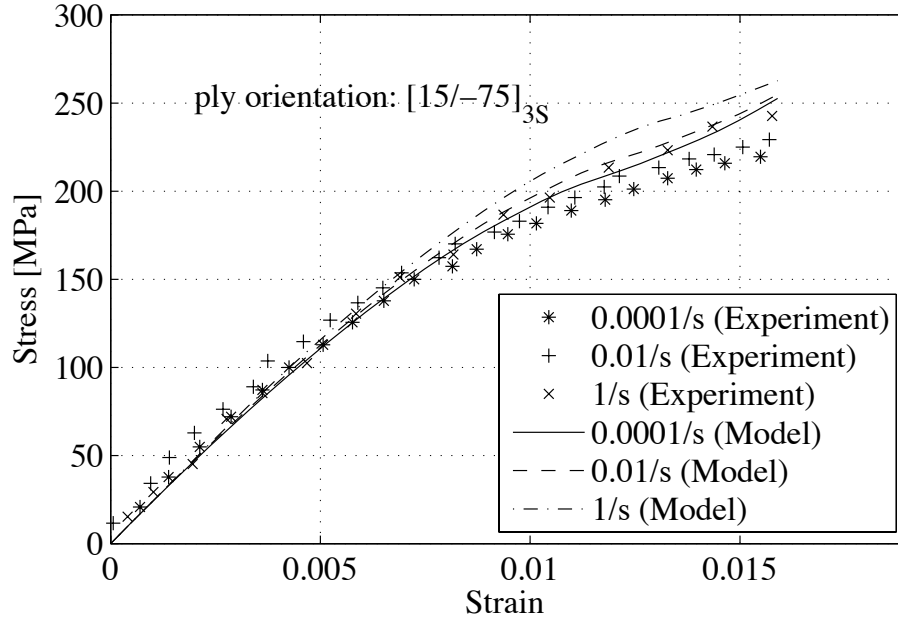


Figure 16: Simulated and experimental uniaxial tensile stress strain curves for the $[+15/-75]_{3S}$ S2-glass laminate at various strain rates.

6 Acknowledgements

The financial supports of National Science Foundation under grants CMS-0310596, 0303902, 0408359, Rolls-Royce contract 0518502, Automotive Composite Consortium contract 606-03-063L, and AFRL/MNAC MNK-BAA-04-0001 contract are gratefully acknowledged. The first author would like to acknowledge the faculty start-up funds provided by Vanderbilt University.

References

- [1] C. Oskay and J. Fish. Eigendeformation-based reduced order homogenization for failure analysis of heterogeneous materials. *Comp. Meth. Appl. Mech. Engng.*, 196:1216–1243, 2007.
- [2] J. Fish, K. L. Shek, M. Pandheeradi, and M. S. Shephard. Computational plasticity for composite structures based on mathematical homogenization: Theory and practice. *Comput. Meth. Appl. Mech. Engng.*, 148:53–73, 1997.
- [3] J. Fish and K. L. Shek. Finite deformation plasticity of composite structures: Computational models and adaptive strategies. *Comput. Meth. Appl. Mech. Engng.*, 172:145–174, 1999.
- [4] J. Fish, Q. Yu, and K. L. Shek. Computational damage mechanics for composite materials based on mathematical homogenization. *Int. J. Numer. Meth. Engng.*, 45:1657–1679, 1999.
- [5] G. J. Dvorak. Transformation field analysis of inelastic composite materials. *Proc. R. Soc. Lond. A*, 437:311–327, 1992.

- [6] J. C. Michel and P. Suquet. Nonuniform transformation field analysis. *Int. J. Solids Structures*, 40:6937–6955, 2003.
- [7] J. C. Michel and P. Suquet. Computational analysis of nonlinear composite structures using the nonuniform transformation field analysis. *Comput. Meth. Appl. Mech. Engng.*, 193:5477–5502, 2004.
- [8] I. Babuska and J. T. Oden. Verification and validation in computational engineering and science: Basic concepts. *Comp. Meth. Appl. Mech. Engng.*, 193:4057–4066, 2004.
- [9] N. Lahellec, F. Mazerolle, and J. C. Michel. Second-order estimate of the macroscopic behavior of periodic hyperelastic composites: Theory and experimental validation. *J. Mech. Phys. Solids*, 52:27–49, 2004.
- [10] R. Jeryan, C. D. Warren, J. Carpenter, and P. S. Sklad. Composite crash energy management. In *Automotive Lightweighting Materials, FY2004 Progress Report*. Department of Energy, 2004.
- [11] D. E. Goldberg. *Genetic Algorithms in Search, Optimization and Machine Learning*. Addison-Wesley, Reading, MA, 1989.
- [12] Z. Michalewicz. *Genetic Algorithms+Data Structures=Evolution Programs*. Springer, Berlin, 1992.
- [13] P. M. Suquet. Elements of homogenization for inelastic solid mechanics. In E. Sanchez-Palencia and A. Zaoui, editors, *Homogenization Techniques for Composite Media*. Springer-Verlag, 1987.
- [14] K. Terada and N. Kikuchi. Nonlinear homogenization method for practical applications. In S. Ghosh and M. Ostoja-Starzewski, editors, *Computational Methods in Micromechanics*, volume AMD-212/MD-62, pages 1–16. ASME, 1995.
- [15] F. Feyel and J.-L. Chaboche. Fe2 multiscale approach for modelling the elastoviscoplastic behavior of long fiber sic/ti composite materials. *Comput. Methods Appl. Mech. Engng.*, 183:309–330, 2000.
- [16] J. C. Simo and J. W. Ju. Strain- and stress-based continuum damage models - i. formulation. *Int. J. Solids Structures*, 23(7):821–840, 1987.
- [17] J.-F. Dube, G. Pijaudier-Cabot, and C. La Borderie. Rate dependent damage model for concrete in dynamics. *J. Engng. Mech.*, 122(10):939–947, 1996.
- [18] P. Lipetzky, G. J. Dvorak, and N. S. Stoloff. Tensile properties of a sic/sic composite. *Mater. Sci. Eng.*, A216:11–19, 1996.
- [19] L. Ianucci. Progressive failure modelling of woven carbon composite under impact. *Int. J. Impact Engng.*, 32:1013–1043, 2006.
- [20] K. Kim and G. Z. Voyiadjis. Non-linear finite element analysis of composite panels. *Composites: Part B*, 30:365–381, 1999.
- [21] P. Perzyna. Fundamental problems in viscoplasticity. *Adv. Appl. Mech.*, 9:244–368, 1966.
- [22] C. Griswold, W. M. Cross, L. Kjerengtroen, and J. J. Kellar. Interphase variation in silane-treated glass-fiber-reinforced epoxy composites. *J. Adhesion Sci. Technol.*, 19(3-5):279–290, 2005.
- [23] J. Fish. Bridging the scales in nano engineering and science. *J. Nanoparticle Research*, 8:577–594, 2006.

- [24] J. E. Jr. Dennis and R. B. Schnabel. *Numerical Methods for Unconstrained Optimization and Nonlinear Equations*, volume 16 of *Classics in Applied Mathematics*. SIAM, Philadelphia, PA, 1996.
- [25] J. J. More. The Levenberg-Marquardt algorithm: Implementation and theory. In G. A. Watson, editor, *Numerical Analysis*, number 630 in *Lecture Notes in Math.*, pages 105–116. Springer-Verlag, 1977.
- [26] *IMSL Math/Library Volumes 1 and 2 User's Manual*. Visual Numerics, 1997.
- [27] P. E. Gill and W. Murray. Minimization subject to bounds on the variables. Technical Report NAC72, National Physical Laboratory, England, 1976.
- [28] P. Charbonneau and B. Knapp. A user's guide to PIKAIA 1.0. NCAR technical note, National Center for Atmospheric Research, 1996.
- [29] A. Ibrahimbegovic, C. Knopf-Lenoir, A. Kucerova, and P. Villon. Optimal design and optimal control of structures undergoing finite rotations and elastic deformations. *Int. J. Numer. Meth. Engng.*, 61:2428–2460, 2004.
- [30] O. Hrstka and A. Kucerova. Improvements of real coded genetic algorithms based on differential operators preventing premature convergence. *Adv. Engng. Software*, 35:237–246, 2004.
- [31] D. Brewer. "HSR/EPM combustor materials development program". *Mater. Sci. Eng.*, A261:284–291, 1999.
- [32] M. Verilli, R. C. Robinson, A. M. Calomino, and D. J. Thomas. Ceramic matrix composite vane subelement testing in a gas turbine environment. In *Proceedings of ASME Turbo Expo 2004*, number GT2004-53970, Vienna, Austria, June 14-17 2004.
- [33] G. N. Morscher and V. V. Pujar. Melt-infiltrated sic composites for gas turbine engine applications. In *Proceedings of 49th ASME IGTI Power for Land, Sea and Air*, number GT2004-53196, Vienna, Austria, June 14-17 2004.
- [34] S. J. Zinkle and L. L. Snead. Thermophysical and mechanical properties of sic/sic composites in fusion materials. Progress Report for Period Ending June 30 1998 DOE/ER-0313/24, Oak Ridge National Laboratory, 1998.
- [35] S. V. Thiruppukuzhi and C. T. Sun. Models for the strain-rate-dependent behavior of polymer composites. *Compos. Sci. Technol.*, 61:1–12, 2001.
- [36] *Assessment of Research Needs for Wind Turbine Rotor Materials Technology*. National Academies Press, 1991.

Appendix: Coefficient Tensors

The coefficient tensors for the $(m + n)$ point model are functions of elastic (G_{ijkl}) , phase (g_{ijkl}^{ph}) , and interface (g_{ijk}^{int}) polarization functions, in addition to the elastic properties of the microconstituents. The expressions for the coefficient tensors are given as:

$$\bar{L}_{ijkl} = \frac{1}{|\Theta|} \int_{\Theta} L_{ijmn}(\mathbf{y}) A_{mnkl}(\mathbf{y}) d\mathbf{y} \quad (38)$$

$$\bar{\mathbf{R}}_{ij}^{(\beta)} = \frac{1}{|\Theta|} \int_{\Theta} L_{ijkl}(\mathbf{y}) \tilde{\mathbf{R}}_{kl}^{(\beta)}(\mathbf{y}) d\mathbf{y} \quad (39)$$

$$\bar{M}_{ijkl}^{(\gamma)} = \frac{1}{|\Theta|} \int_{\Theta} L_{ijmn}(\mathbf{y}) \left(\tilde{P}_{kl ij}^{(\gamma)}(\mathbf{y}) - I_{kl ij} N_{\text{ph}}^{(\gamma)}(\mathbf{y}) \right) d\mathbf{y} \quad (40)$$

$$\hat{\mathbf{C}}_{ij}^{(\alpha)} = \frac{1}{|S^{(\alpha)}|} \int_{S^{(\alpha)}} \int_{\Theta} g_{mnp}^{\text{int}}(\mathbf{y}, \hat{\mathbf{y}}) L_{mnkl}(\mathbf{y}) A_{kl ij}(\mathbf{y}) \hat{\mathbf{e}}_p(\hat{\mathbf{y}}) d\mathbf{y} d\hat{\mathbf{y}} \quad (41)$$

$$\hat{\mathbf{D}}^{(\alpha\beta)} = \frac{1}{|S^{(\alpha)}|} \int_{S^{(\alpha)}} \int_{\Theta} g_{mnp}^{\text{int}}(\mathbf{y}, \hat{\mathbf{y}}) L_{mnkl}(\mathbf{y}) \tilde{\mathbf{R}}_{kl}^{(\beta)}(\mathbf{y}) \otimes \hat{\mathbf{e}}_p(\hat{\mathbf{y}}) d\mathbf{y} d\hat{\mathbf{y}} \quad (42)$$

$$\hat{\mathbf{F}}_{ij}^{(\alpha\gamma)} = \frac{1}{|S^{(\alpha)}|} \int_{S^{(\alpha)}} \int_{\Theta} g_{mnp}^{\text{int}}(\mathbf{y}, \hat{\mathbf{y}}) L_{mnkl}(\mathbf{y}) \left(\tilde{P}_{kl ij}^{(\gamma)}(\mathbf{y}) - I_{kl ij} N_{\text{ph}}^{(\gamma)}(\mathbf{y}) \right) \hat{\mathbf{e}}_p(\hat{\mathbf{y}}) d\mathbf{y} d\hat{\mathbf{y}} \quad (43)$$

$$P_{ijkl}^{(\eta\gamma)} = \frac{1}{|\Theta^{(\eta)}|} \int_{\Theta^{(\eta)}} \tilde{P}_{ijkl}^{(\gamma)}(\mathbf{y}) d\mathbf{y} \quad (44)$$

$$A_{ijkl}^{(\eta)} = \frac{1}{|\Theta^{(\eta)}|} \int_{\Theta^{(\eta)}} A_{ijkl}(\mathbf{y}) d\mathbf{y} \quad (45)$$

$$\hat{\mathbf{R}}_{ij}^{(\eta\beta)} = \frac{1}{|\Theta^{(\eta)}|} \int_{\Theta^{(\eta)}} \tilde{\mathbf{R}}_{ij}^{(\beta)}(\mathbf{y}) d\mathbf{y} \quad (46)$$

$$\tilde{P}_{ijkl}^{(\eta)}(\mathbf{y}) = \int_{\Theta^{(\eta)}} g_{ijkl}^{\text{ph}}(\mathbf{y}, \hat{\mathbf{y}}) d\hat{\mathbf{y}} \quad (47)$$

$$\tilde{\mathbf{R}}_{ij}^{(\alpha)}(\mathbf{y}) = \int_{\bar{S}^{(\alpha)}} g_{ijp}^{\text{int}}(\mathbf{y}, \hat{\mathbf{y}}) N_{\text{int}}^{(\alpha)}(\hat{\mathbf{y}}) \hat{\mathbf{e}}_p(\hat{\mathbf{y}}) d\hat{\mathbf{y}} \quad (48)$$

where $\hat{\mathbf{e}}$ are the basis vectors in the local normal and tangential directions along the interface; $N_{\text{ph}}^{(\gamma)}$ and $N_{\text{int}}^{(\alpha)}$ are phase partition and interface partition shape functions. The selection of appropriate shape functions are provided in [1]. The polarization functions are obtained by solving influence function problems given below

Elastic Influence Function (EIF) Problem:

Given $L_{ijmn}(\mathbf{y})$, find $H_{ikl}(\mathbf{y}) : \bar{\Theta} \rightarrow \mathbb{R}$ such that:

$$\begin{aligned} \{L_{ijmn}(\mathbf{y}) A_{mnkl}(\mathbf{y})\}_{,y_j} &= 0; \quad \mathbf{y} \in \Theta \\ A_{ijkl}(\mathbf{y}) &= I_{ijkl} + G_{ijkl}(\mathbf{y}); \quad G_{ijkl}(\mathbf{y}) = H_{(i,y_j)kl}(\mathbf{y}) \\ \Theta &- \text{periodic boundary conditions on } \mathbf{y} \in \Gamma_\Theta \end{aligned}$$

Phase Damage Influence Function (PDIF) Problem:

Given $L_{ijmn}(\mathbf{y})$, find $h_{ikl}^{\text{ph}}(\mathbf{y}, \hat{\mathbf{y}}) : \bar{\Theta} \times \bar{\Theta} \rightarrow \mathbb{R}$ such that:

$$\begin{aligned} \left\{L_{ijmn}(\mathbf{y}) \left(g_{mnkl}^{\text{ph}}(\mathbf{y}, \hat{\mathbf{y}}) + I_{mnkl}d(\mathbf{y} - \hat{\mathbf{y}})\right)\right\}_{,y_j} &= 0; \quad \mathbf{y}, \hat{\mathbf{y}} \in \Theta \\ g_{ijkl}^{\text{ph}}(\mathbf{y}, \hat{\mathbf{y}}) &= h_{(i,y_j)kl}^{\text{ph}}(\mathbf{y}, \hat{\mathbf{y}}) \\ \Theta &- \text{periodic boundary conditions on } \mathbf{y} \in \Gamma_\Theta \\ \llbracket h_{ikl}^{\text{ph}} \rrbracket(\mathbf{y}, \hat{\mathbf{y}}) &= 0 \quad \text{on } \mathbf{y}, \hat{\mathbf{y}} \in \Theta \end{aligned}$$

Interface Damage Influence Function (IDIF) Problem:

Given $L_{ijmn}(\mathbf{y})$, find $h_{ip}^{\text{int}}(\mathbf{y}, \hat{\mathbf{y}}) : \bar{\Theta} \times S \rightarrow \mathbb{R}$ such that:

$$\begin{aligned} \{L_{ijmn}(\mathbf{y}) g_{mnp}^{\text{int}}(\mathbf{y}, \hat{\mathbf{y}})\}_{,y_j} &= 0; \quad \mathbf{y} \in \Theta, \quad \hat{\mathbf{y}} \in S \\ g_{ijp}^{\text{int}}(\mathbf{y}, \hat{\mathbf{y}}) &= h_{(i,y_j)p}^{\text{int}}(\mathbf{y}, \hat{\mathbf{y}}) \\ \Theta &- \text{periodic boundary conditions on } \mathbf{y} \in \Gamma_\Theta \\ \llbracket h_{ip}^{\text{int}} \rrbracket(\mathbf{y}, \hat{\mathbf{y}}) &= Q_{ip}d(\mathbf{y} - \hat{\mathbf{y}}) \quad \text{when } \mathbf{y} \in S \text{ or } \hat{\mathbf{y}} \in S \end{aligned}$$

in which, d is Dirac delta; Γ_Θ denotes boundaries of the unit cell; and $\llbracket \cdot \rrbracket$ is the jump operator.